International Journal of Nanomedicine

Dovepress
open access to scientific and medical research

Open Access Full Text Article

ORIGINAL RESEARCH

A pH-Responsive Drug-Delivery System Based on Apatinib-Loaded Metal-Organic Frameworks for Ferroptosis-Targeted Synergistic Anti-Tumor Therapy

Fengyi Yang[1,2,*], Qiaoyan Dong[3,*], Zhuo Chen[1,2,*], Benjian Gao[1,2,*], Dongning Zheng[1,2], Rui Wang[1,2], Shu Qin[1,2], Fangyi Peng[1,2], Ming Luo[1,2], Jin Yang[1,2], Mengmei Nie[4], Bo Li[1,2], Xiaoli Yang[1,2]

[1]Department of General Surgery (Hepatopancreatobiliary Surgery), The Affiliated Hospital of Southwest Medical University, Luzhou, 646000, People's Republic of China; [2]Academician (Expert) Workstation of Sichuan Province, Metabolic Hepatobiliary and Pancreatic Diseases Key Laboratory of Luzhou City, The Affiliated Hospital of Southwest Medical University, Luzhou, 646000, People's Republic of China; [3]Luzhou Senior High School, Luzhou, 646000, People's Republic of China; [4]Department of Urological Surgery, The Affiliated Hospital of Southwest Medical University, Luzhou, 646000, People's Republic of China

*These authors contributed equally to this work

Correspondence: Bo Li; Xiaoli Yang, Email liboer2002@126.com; 344920646@qq.com

---

Purpose: The efficacy of systemic therapy for hepatocellular carcinoma (HCC) is limited mainly by the complex tumor defense mechanism and the severe toxic side-effects of drugs. The efficacy of apatinib (Apa), a key liver cancer treatment, is unsatisfactory due to inadequate targeting and is accompanied by notable side-effects. Leveraging nanomaterials to enhance its targeting represents a crucial strategy for improving the effectiveness of liver cancer therapy.

Patients and Methods: A metal polyphenol network-coated apatinib-loaded metal-organic framework-based multifunctional drug-delivery system (MIL-100@Apa@MPN) was prepared by using metal-organic frameworks (MOFs) as carriers. The nanoparticles (NPs) were subsequently characterized using techniques such as X-ray diffraction (XRD), transmission electron microscopy (TEM), zeta potential measurements, and particle size analysis. In vitro experiments were conducted to observe the drug release kinetics and cytotoxic effects of MIL-100@Apa@MPN on HepG2 cells. The in vivo anti-tumor efficacy of MIL-100@Apa@MPN was evaluated using the H22 tumor-bearing mouse model.

Results: The formulated MIL-100@Apa@MPN demonstrates remarkable thermal stability and possesses a uniform structure, with measured drug-loading (DL) and encapsulation efficiency (EE) rates of 28.33% and 85.01%, respectively. In vitro studies demonstrated that HepG2 cells efficiently uptake coumarin-6-loaded NPs, and a significant increase in cumulative drug release was observed under lower pH conditions (pH 5.0), leading to the release of approximately 73.72% of Apa. In HepG2 cells, MIL-100@Apa@MPN exhibited more significant antiproliferative activity compared to free Apa. In vivo, MIL-100@Apa@MPN significantly inhibited tumor growth, attenuated side-effects, and enhanced therapeutic effects in H22 tumor-bearing mice compared to other groups.

Conclusion: We have successfully constructed a MOF delivery system with excellent safety, sustained-release capability, pH-targeting, and improved anti-tumor efficacy, highlighting its potential as a therapeutic approach for the treatment of HCC.

Keywords: metal-organic frameworks nanoparticles, apatinib, drug-targeting delivery, ferroptosis therapy, hepatocellular carcinoma

---

Introduction

Hepatocellular carcinoma (HCC) is the third leading cause of cancer-related deaths worldwide.[1] Currently, targeted therapy is the primary treatment modality for HCC, with apatinib (Apa) being the most representative drug.[2] Apa is a highly specific inhibitor of the vascular endothelial growth factor receptor 2 (VEGFR2) tyrosine kinase complex, demonstrating a strong anti-angiogenic effect.[3–5] However, it lacks target specificity, leading to frequent severe adverse

Received: 8 May 2024
Accepted: 28 August 2024
Published: 4 September 2024

effects, such as hand-foot syndrome, hypertension, and proteinuria. When used as a monotherapy for targeting HCC, Apa showed a modest improvement in median overall survival (OS), with an increase of just 1.9 months.[6] Its objective remission rate (ORR) was only 15.73%.[7] Therefore, there is an urgent need to enhance the targeting capabilities of Apa.

Metal-organic frameworks (MOFs) have allured considerable attraction in light of their porous structure, which renders them versatile for use in catalysis, drug encapsulation, and drug-delivery applications.[8–11] Iron-based MOF (MIL-100) is receiving extensive attention due to its high porosity and effective drug-loading, promising potential for applications in biomedicine as well as favorable in vitro/vivo toxicological profiles and biodegradability.[12–14] MIL-100 is degraded in the acidic microenvironment of HCC, thereby facilitating precise transportation of drug into the tumor and enhancing its targeting efficiency, while minimizing undesirable side-effects. Additionally, MIL-100 can release Fe ions, which induce ferroptosis.[15–17] The sensitivity of tumor cells to Apa can be enhanced by utilizing ferroptosis inducers.[18] Furthermore, Apa has the ability to trigger ferroptosis by inhibiting VEGFR2/Nrf2/Keap1 activation and its downstream pathways.[19] Thus, there is a reciprocal amplification mechanism between Apa and ferroptosis, resulting in a synergistic enhancement of their effectiveness in promoting tumor suppression. Hence, the combination of ferroptosis inducers and Apa holds promise as an innovative approach to cancer treatment. Given its exceptional bioinertness and in vivo biodegradability, MIL-100 represents an excellent platform for the co-delivery of Fe^{3+} and Apa.

Within the scope of this study, we introduced a versatile drug-delivery system designed for synergistic therapy targeting tumor-specific ferroptosis and Apa. MIL-100 was utilized as both the iron source for ferroptosis therapy and the carrier for loading Apa. The nanostructures were coated with the polyphenol tannic acid (TA) to form a metal polyphenol network (MPN) covering in combination with Fe^{3+}. This study represents the first instance of employing metal cations in MIL-100 for the direct formation of MPN with TA. The MPN demonstrated pH responsiveness and was shown to effectively prevent drug leakage, making it an ideal component for the final nanogenerator (MIL100@Apa@MPN). The pH-sensitive MPN underwent dissociation in an acidic pH environment with ferroptosis therapy described by the following equations:[20]

$$\mathrm{Fe}^{3+} + \mathrm{GSH} \rightarrow \mathrm{Fe}^{2+} + \mathrm{GSSG} \tag{1}$$

$$\mathrm{Fe}^{2+} + \mathrm{H_2O_2} \rightarrow \mathrm{Fe}^{3+} + (\mathrm{OH}) - + \cdot \mathrm{OH} \tag{2}$$

Therefore, the nanogenerator MIL100@Apa@MPN was found to show promising potential as a strategy to enhance the synergistic efficacy of tumor-targeted ferroptosis and Apa therapy. Our research provides a platform for further exploration of strategies for constructing a synergistic system that utilizes MOFs and Apa, thereby expanding the biological applications of MOFs.

Materials and Methods

Materials

Iron (III) chloride hexahydrate ($FeCl_3 \cdot 6H_2O$), benzene tricarboxylic acid (BTC), hydrogen nitrate (HNO_3), and potassium fluoride (KF) were purchased from Shanghai Acmec Biochemical Technology Co., Ltd. (Shanghai, China), TA were purchased from Shanghai Macklin Biochemical Technology Co., Ltd. (Shanghai, China). Apa was provided by Southwest Medical University (Luzhou, China). Ferrostatin-1 was purchased from MedChemexpress (USA). GSH/GSSG Ratio Detection Assay kit were purchased from Beyotime Biochemical Technology Co., Ltd. (Jiangsu, China). Hydrogen peroxide (H_2O_2) test kit were purchased from Beijing Solarbio Science & Technology Co.,Ltd. (Beijing, China). Vitamin E was purchased from Shanghai Macklin Biochemical Co., Ltd. Cell counting kit-8 (CCK-8) was obtained from Bioground (Shanghai, China). All reagents were analytical grade and used as received without further purification.

The human hepatoma cell line (HepG2) and murine hepatoma cell line (H22) were were purchased from Procell Life Science and Technology Co. (Wuhan, China), Ltd. HepG2 cells were cultured in Dulbecco's modified Eagle's medium (DMEM), supplemented with 10% fetal bovine serum (FBS; Gibco, Grand Island, NY, USA), and 1% penicillin–streptomycin. H22 cells were cultured in RPMI-1640 medium (Gibco) supplemented with 10% FBS and 1% penicillin

−streptomycin. All cells were cultured at 37°C in a humidified atmosphere containing 5% CO_2. The HepG2 cells and H22 cells were verified by short tandem repeat (STR) profiling.

C57BL/6 mice (aged 4–6 weeks old, approximately 20 g) were housed under normal conditions (20–22 °C, 50% relative humidity) with 12-h light/dark cycles and given free access to food and water. All mice exhibited a state of well-being, with no instances of infections documented throughout the duration of the experiment. The use and handling of mice adhered to ethical guidelines outlined in the National Institutes of Health Guide for the Care and Use of Laboratory Animals. All experimental protocols involving animal subjects received approval from the Institutional Animal Care and Treatment Committee of Southwest Medical University (swmu20240009).

Synthesis of MIL-100 Nanoparticles (NPs)

MIL-100 was synthesized according to a previously reported method, with slight modifications.[21] Briefly, $FeCl_3 \cdot 6H_2O$ (811 mg, 3 mmol), BTC (420 mg, 2 mmol), HNO_3 (3 mmol), KF (174 mg, 3 mmol), and water (20 mL) were combined in a 50-mL Teflon-lined stainless-steel container and sealed. The mixture was heated at 120°C for 24 h to obtain MIL-100. The product was then washed three times with 50 mL each of water and ethanol. The resulting yellow powder was dispersed in ethanol and dried at 60°C.

Synthesis of MIL-100@Apa@MPN NPs

MIL-100 (2 mg) was combined with Apa (1 mg) in 5 mL water. The mixture was stirred for 24 h and the resulting product, MIL-100@Apa, was washed with ethanol and dried at 60°C for 6 h.

TA (40 mg) in 10 mL of water was added to an aqueous suspension of MIL-100@Apa NPs (0.4 mg mL^{-1} MIL-100@Apa and 4 mg mL^{-1} TA). The suspension was vortexed vigorously for 15 min. The colloidal particles were then subjected to three cycles of centrifugation (12,000 rpm, 5 min) and redispersion, using Milli-Q water, to eliminate any excess TA and Fe^{3+}. The resulting MIL-100@Apa@MPN was re-dispersed in 1 mL of Milli-Q water and dried at 60°C for 6 h.

Characterization of the MIL-100@Apa@MPN NPs

A D8 ADVANCE X-ray diffractometer (Bruker, Germany) was used for Powder X-ray diffraction (XRD) patterns. A zeta potential and particle size analyzer (Zetasizer Nano ZS90, UK) was used for the nanoparticle size distribution and zeta potential. Transmission electron microscopy (TEM) was utilized to acquire images for both transmission electron microscopy and elemental mapping (FEI Talos F200X, Thermo Fisher Scientific, USA). The X-ray photoelectron spectroscopy (XPS) was employed for the analysis of the valence state of elements by using ESCALAB 250XI (Thermo Fisher Scientific, USA). N2 adsorption/desorption and pore-size distribution analyses were conducted using the ASAP 2460 apparatus (ASAP 2460, USA). The Brunauer−Emmett−Teller (BET) method was used to evaluate the surface area of the NPs. Ultraviolet-visible (UV-vis) spectra were recorded using a UV-vis spectrophotometer (UV-3600, Japan). Fourier transform infrared (FT-IR) spectrophotometer (Nicolet 6700-Continuμm, Thermo Fisher Scientific, USA) was used for FT-IR spectra measure. Thermogravimetric analysis (TGA) was performed to evaluate the loading capacity of the NPs (METTLER TG-DSC 3+, Switzerland).

Entrapment Efficiency (EE%) and Drug-Loading (DL%)

The MIL-100@Apa preparation was centrifuged (12,000 rpm, 5 min) and the supernatant collected for subsequent quantitative analysis. Apa was quantified by photometer absorption spectroscopy using a standard curve established by measuring varying concentrations of Apa and recording the highest absorption peak at 347 nm. The standard curve was fitted according to the following equation: $Y = 0.0062X+0.1516$, $R^2 = 0.9988$. DL and EE were calculated using the following equations:

$$DL = \frac{\text{weight of the drug}}{\text{weight of the nanoparticles}} \times 100\% \tag{3}$$

$$EE = \frac{\text{Actual drug loading}}{\text{Theoretical drug loading}} \times 100\% \quad (4)$$

In vitro Cellular Uptake of NPs

To assess the cellular uptake of MIL-100@MPN NPs by HepG2 cells, coumarin-6 fluorescent-loaded MIL-100@MPN NPs were synthesized using the aforementioned method. Coumarin-6 (C6) loaded MIL-100@MPN NPs were prepared according to the same method employed for the synthesis of MIL-100@Apa@MPN NPs. The HepG2 cells were seeded into a 24-well plate (1×10^5 cells per well) and incubated for 24 h at 37°C. Subsequently, the cells were treated with medium containing 500 μg/mL blank NPs, 100 μg/mL free C6, or MIL-100@C6@MPN (equivalent to 100 μg/mL free C6), and further incubated for 2 h. Subsequently, the cells were examined using a fluorescence microscope (Olympus, Tokyo, Japan).

In vitro Drug Release Behavior

The release of Apa release from MIL-100@Apa@MPN NPs at 37°C was assessed by dispersing the samples in 10 mL phosphate-buffered saline (PBS) adjusted to pH 5.0 and 7.4 with gentle shaking. For each measurement, a 0.6 mL solution was extracted by centrifugation (12,000 rpm, 5 min). The quantity of Apa released was quantified at 347nm using an ultraviolet spectrophotometer (Hitachi Ltd., Hitachi, Japan).

In vitro Cytotoxicity Assay

For in vitro therapy, the viability of cells was assessed using the cell counting kit-8 (CCK-8) method. HepG2 cells were seeded in a 96-well plate (5×10^3 cells per well) and cultured in DMEM (Gibco) for 24 h at 37°C. Subsequently, the cells were divided into five groups as follows: control, MIL-100@MPN, MIL-100@Apa, free Apa, and MIL-100@Apa@MPN groups. In each group, BPs were added to the cells at concentrations ranging from 1 μg/mL to 100 μg/mL and incubated for 24 h. The cells were then washed three times with DMEM before the addition of a 10% CCK-8 solution (Bioground, China) and incubation for 2 h at 37°C under 5% CO_2. The absorbance of each well was then measured at 450 nm using a Thermo Scientific Microplate Reader.

For ferroptosis therapy, HepG2 cells were cultured in 96-well plates (5×10^3 cells per well) treated with MIL-100@MPN (50 μg/mL) in the presence of various inhibitors of ferroptosis (100 μmol/L Vitamin E and Ferrostatin-1) for 24 h at 37°C under 5% CO_2. The cells were washed three times with DMEM before the addition of a 10% CCK-8 solution. After incubation for 2 h at 37°C under 5% CO_2, the absorbance at 450 nm was quantified using a Thermo Scientific Microplate Reader.

In vivo Antitumor Activity

To establish H22-bearing mouse models, 100 μL H22 cell suspension (1×10^7/mL) was injected subcutaneously into the right thigh of C57BL/6 mice (aged 4–6 weeks, approximately 20 g). Once the solid tumors reached a volume of 150–200 mm^3 by using a caliper, the mice were randomly assigned into four groups (n = 5 per group) as follows: (1) PBS (pH 7.4), (2) MIL-100@MPN, (3) free Apa (10 mg/kg), and (4) MIL-100@Apa@MPN (equivalent to 10 mg/kg free Apa). Treatment was initiated on day 0. Subsequently, the mice received injections (0.1 mL) of the respective formulations once a week three weeks. Mouse weight (measured using a precision balance) and tumor (measured using a digital caliper) were assessed every 3 days over a 21-day period. Following the conclusion of the experiment, euthanasia of the mice was conducted by administering a lethal dose of pentobarbital sodium (150mg/kg) through intraperitoneal injection, the tumors were excised from the mice, photographed, and weighed. The tumor size was determined using the following formula: $V = (a \times b^2)/2$, where a represents the length of the tumor and b represents the width of the tumor.

Histological and Immunohistochemical Analysis

The tumors and vital organ (heart, liver, spleens, lung, and kidney) tissue specimens were dissected and sectioned for hematoxylin and eosin (H&E) staining, followed by examination and photography using optical microscopy. Tumors were also for immunohistochemical (IHC) staining, sections were then incubated with anti-mouse Ki-67, CD31, GPX4 and caspase-3 protein antibodies (GB111141, GB113151, GB114327, GB11009-1, Servicebio, China) for microscopic observation. Apoptosis was detected in tumor tissues using a TdT-mediated dUTP nick-end labeling (TUNEL) apoptosis detection kit according to the Bioground manufacturer's instructions.

Statistical Analysis

Statistical analysis was conducted utilizing GraphPad Prism version 9.5.1 software using two-sided Student's *t*-tests (GraphPad Software, San Diego, CA, USA). All experiments were conducted with triplicate or greater number of specimens. Data were presented as the mean standard deviation (SD). A P-value of < 0.05 was considered to indicate statistical significance.

Results

Characterization of MIL-100@Apa@MPN

MIL-100@Apa@MPN was formed based on the procedure depicted in Figure 1. The MIL-100 nanostructure was initially produced using a simple one-pot method. PXRD analysis was conducted to validate the successful formation of the desired MIL-100 structure (Figure 2A). TGA was conducted on MIL-100 under a nitrogen atmosphere. Demonstrated by Figure S1, the TGA curve revealed that the MIL-100 structure remained intact when heated up to approximately 350 °C, indicating a good thermal stability profile. The Apa-loaded MIL-100 nanostructure was covered with TA by jointly coordinating with the Fe^{3+} in MIL-100@Apa to form a MPN shell to generate MIL-100@Apa@MPN. TEM evaluation of the morphology of the synthesized MIL-100 and MIL-100@Apa@MPN materials revealed that the MIL-100 nanostructure (Figure 2B) displayed a distinct polyhedral configuration, while the MIL-100@Apa@MPN nanostructure (Figure 2C) exhibited a comparatively homogeneous spherical morphology. Meanwhile, TEM characterization of MIL-100@Apa confirmed the successful loading of Apa (Figure S3). High-angle annular dark-field scanning transmission electron microscopy (HAADF-STEM) images (Figure 2D) demonstrated the uniform distribution of carbon (C), oxygen (O), and iron (Fe) elements, indicating the homogeneous structure of the final product, MIL-100@Apa@MPN. Dynamic light scattering (DLS) data demonstrated that the average hydrodynamic size of MIL-100 was approximately 175 nm (Figure 2E). MIL-100@Apa@MPN was then synthesized and characterized by DLS size and zeta potential analyses (Figure 2F). The application of TA coating resulted in an augmentation in particle dimensions and elevation of the negative surface charge. The DL and EE of the MIL-100@Apa@MPN-NPs were 28.33% and 85.01%. Importantly, MIL-100 exhibited a substantial surface area of 732.9 m^2

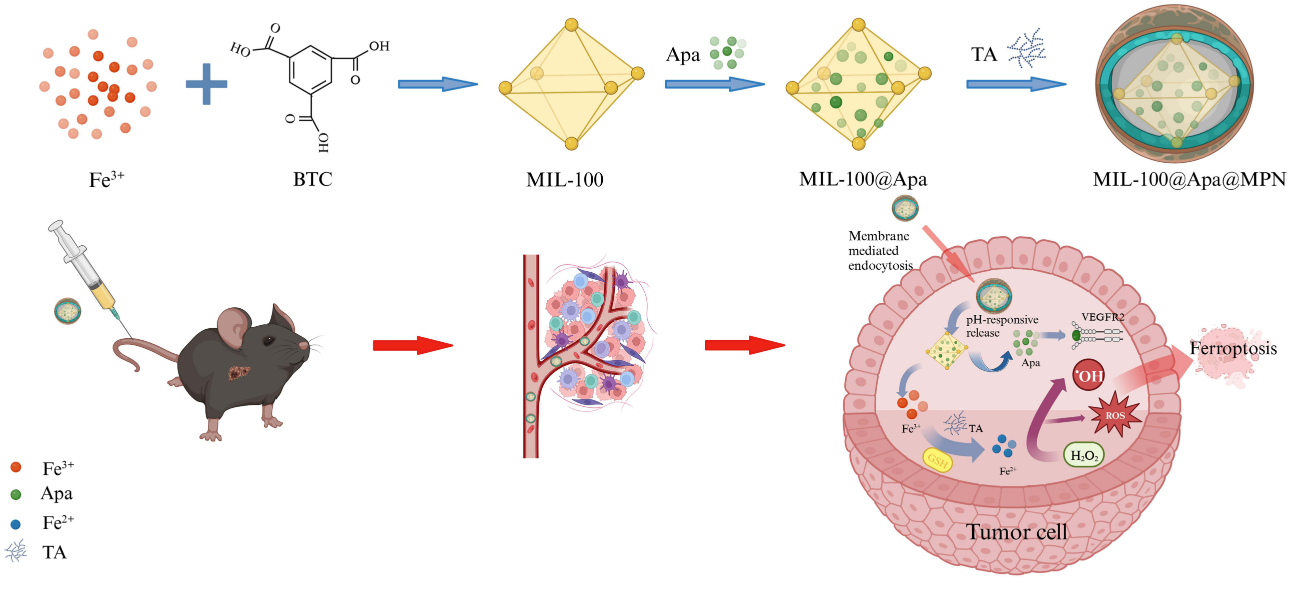

Figure 1 Schematic illustration of the preparation of MIL-100@Apa@MPN and the collaborative therapy for cancer.
Abbreviations: BTC, benzene tricarboxylic acid; Apa, Apatinib; TA, tannic acid; MPN, metal polyphenol network; ROS, reactive oxygen species.

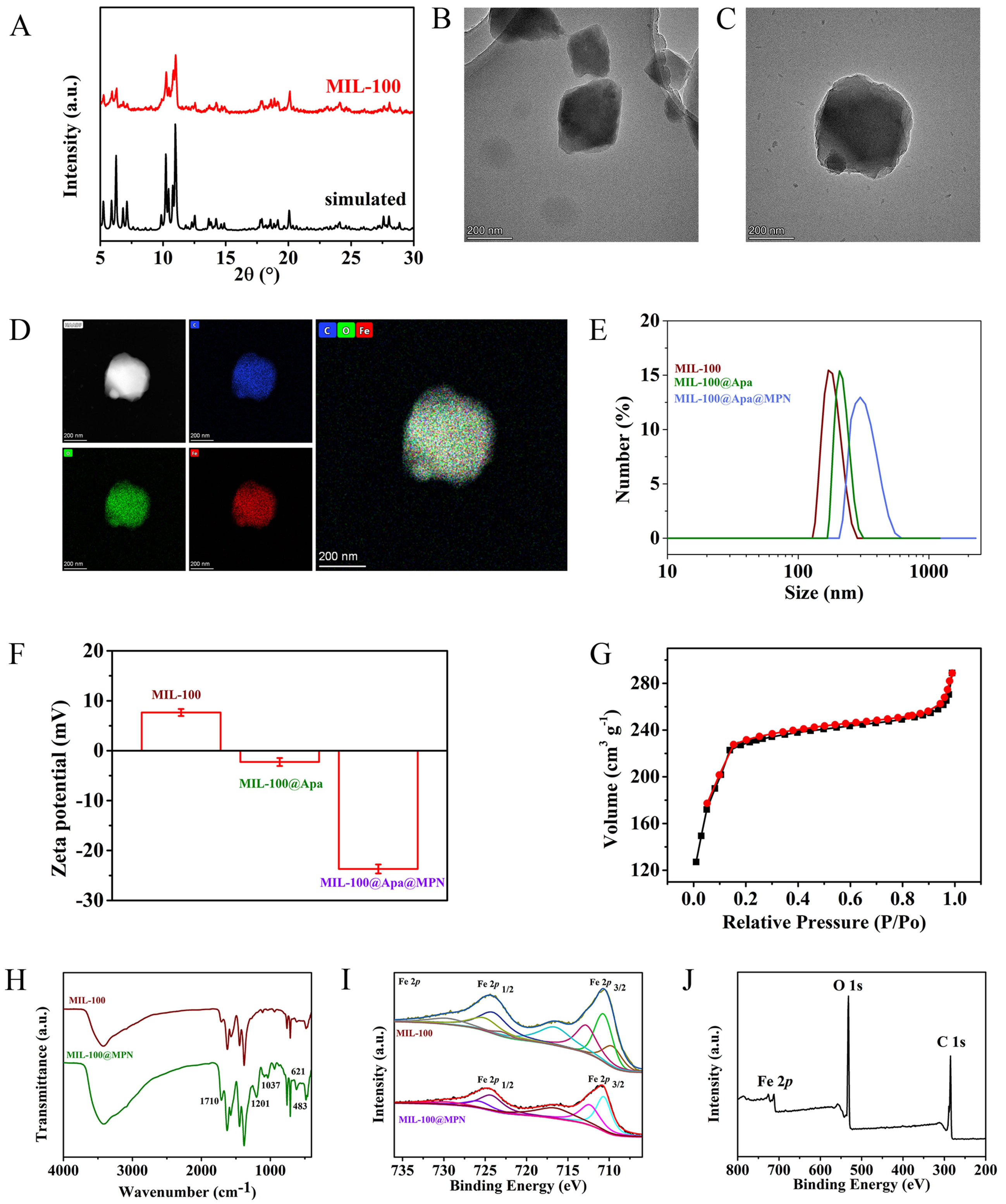

Figure 2 Characterizations of the MIL-100@Apa@MPN NPs.

Notes: (**A**) The PXRD patterns of MIL-100 and patterns simulated from MIL-100 structure. (**B**) TEM images of MIL-100 nanostructures. (**C**) TEM images of MIL-100@Apa@MPN nanostructures. (**D**) Element mapping of MIL-100@Apa@MPN. (**E**) Hydrodynamic sizes (**F**) Zeta potentials of MIL-100, MIL-100@Apa, and MIL-100@Apa@MPN nanoparticles. (n= 3, data are presented as mean ± SD). (**G**) N2 absorption-desorption isotherm of MIL-100. (**H**) FT-IR spectra of MIL-100 and MIL-100@MPN. (**I**) XPS spectrum of Fe 2p in MIL-100 and MIL-100@MPN. (**J**) XPS survey spectrum of MIL-100@MPN nanoparticles.

Abbreviations: PXRD, Powder X-ray diffraction; TEM, Powder X-ray diffraction; Apa, Apatinib; FT-IR, Fourier transform infrared.

g^{-1} (Figure 2G), thereby facilitating drug encapsulation. Apa was incorporated into the nanostructure of MIL-100 via co-incubation, as evidenced by the presence of a characteristic peak at 347 nm in UV-vis spectroscopy (Figure S2).

The generation of MPN in the TA-covered MIL-100 was confirmed by FT-IR spectroscopy (Figure 2H). XPS analysis of the surface chemistry of MIL-100@MPN (Figure 2J) revealed the presence of Fe, C, O, and other elements on the surfaces of MIL-100@MPN. Following curve fitting, the Fe 2p1/2 and Fe 2p3/2 peaks for MIL-100 and MIL-100@MPN (Figure 2I) are located at approximately 710.7, 712.6, 724.1, and 725.4 eV, respectively, indicating the presence of Fe^{3+} species.[22–24]

In vitro Cellular Uptake of NPs

Efficient cellular uptake is pivotal for assessing the efficacy of drug formulations. Following a 2-h cultivation with blank NPs, free C6, and MIL-100@C6@MPN, fluorescence microscopy was employed to capture images to assess cellular uptake in vitro (Figure 3). There was an absence of fluorescence detected in the control (Figure 3) and blank NPs (Figure 3) groups. In contrast, higher fluorescence intensity was detected in the group incubated with MIL-100@C6@MPN (Figure 3) compared to free C6 (Figure 3). This observation indicated the efficient uptake of MIL-100@C6@MPN by HepG2 cells.

In vitro Drug Release Behavior

To evaluate the feasibility of achieving continuous drug release, we investigated The in vitro release pattern of free Apa and MIL-100@Apa@MPN NPs. The drug-release profiles of MIL-100@Apa@MPN NPs incubated at 37°C in PBS buffers adjusted to pH 7.4 and 5.0 are illustrated in Figure 4A. After 2 h, the cumulative drug release of NPs in neutral PBS (pH 7.4) was approximately 15.9%, with the release of Apa remaining relatively constant during this period. After 72 h, the release of Apa reached 42.31%. Conversely, a notable increase in cumulative drug release was observed under lower pH conditions (pH 5.0), resulting in the release of 73.72% of Apa from the NPs. The findings suggest that the MPN coating effectively prevented the release of Apa at pH 7.4, while facilitating its release under more acidic conditions. Thus, the MIL-100@Apa@MPN composite demonstrated a pH-responsive drug-release capability. Due to the acidic nature of the tumor extracellular microenvironment, pH serves as a potent internal stimulus for the initiation of drug release specifically targeted towards cancer cells.

In vitro Cytotoxicity Assay

The cytotoxic activity of various drugs was assessed in HepG2 cells using the CCK-8 method. After incubation with MIL-100@MPN NPs at 100 μg/mL, 74.03% HepG2 cell viability indicated the significant cytotoxic effects of the NPs (Figure 4B). This can be attributed to the natural occurrence of GSH and H_2O_2, which mediate monotherapy of ferroptosis. We utilized the GSH/GSSG Ratio Detection Assay kit to measure the ratio of Glutathione (GSH) to oxidized glutathione (GSSG). The GSH/GSSG values of the MIL-100@MPN and MIL-100@Apa@MPN groups exhibited a significant decrease compared to the PBS and Apa groups (Figure 4C). The hydrogen peroxide (H_2O_2) test kit was used to determine the concentration of H_2O_2, and the results showed a significant decrease in H_2O_2 concentration in the MIL-100@MPN and MIL-100@Apa@MPN groups

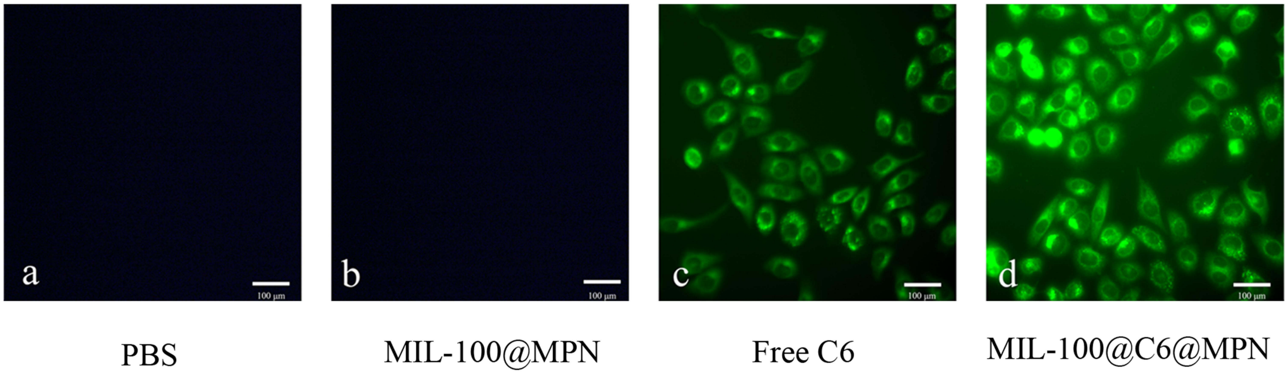

Figure 3 Fluorescent images of HepG2 cells.

Notes: Fluorescent images of HepG2 cells treated with (**a**) control, (**b**) blank nanoparticles, (**c**) free coumarin-6, and (**d**) coumarin-6-loaded nanoparticles for 2 h. Scale bar, 100 μm.

Abbreviations: C6, coumarin-6; MPN, metal polyphenol network.

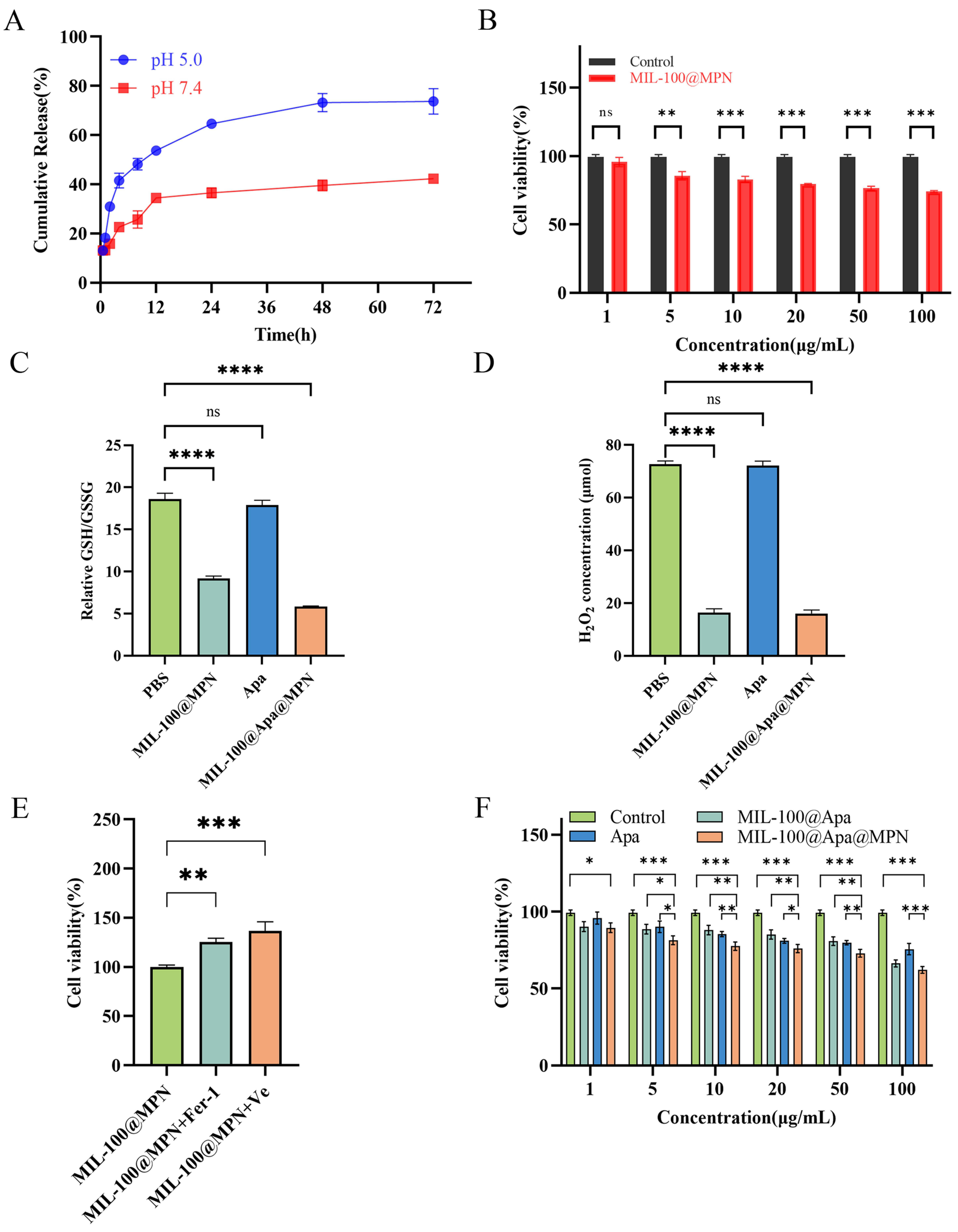

Figure 4 In vitro drug release and cytotoxicity assessment.

Notes: (**A**) The drug-release profiles of MIL-100@Apa@MPN NPs at 37 °C in PBS buffers with varying pH values. (**B**) Cell viabilities of HepG2 cells with PBS and MIL-100@MPN treatments at different concentrations. (**C**) The GSH/GSSG ratio in HepG2 cells. (**D**) Concentration of H_2O_2 (**E**) Cell viabilities of HepG2 cells treated with MIL-100@MPN and different ferroptosis inhibitors. (**F**) Cell viabilities of HepG2 cells with different treatments at different concentrations. Data are presented as mean ± standard deviation (* P < 0.05, ** P < 0.01, *** P < 0.001, **** P < 0.0001).

Abbreviations: Apa, Apatinib; MPN, metal polyphenol network; Fer-1, Ferrostatin-1; Ve, Vitamin e; H_2O_2, hydrogen peroxide; GSH, Glutathione; GSSG, oxidized glutathione.

(Figure 4D). Furthermore, treatment with ferroptosis inhibitors attenuated the efficacy of ferroptosis and led to increased cell viabilities, thus confirming the therapeutic modality of ferroptosis in MIL-100@MPN (Figure 4E). Similarly, the viability of cells treated with various drug formulations demonstrated a dose-dependent response (Figure 4F). Cell proliferation was effectively suppressed in a dose-dependent manner following treatment with various drug formulations. In particular, the synergistic therapy group (MIL-100@Apa@MPN) exerted a more pronounced cytotoxic effect compared to free Apa. This effect reached the level of statistical significance when the concentration of Apa exceeded 100 μg/mL ($P < 0.05$), highlighting the enhanced therapeutic efficacy achieved by MIL-100@Apa@MPN therapy, which combines ferroptosis and targeted therapy modalities.

In vivo Antitumor Activity

We evaluated the in vivo anticancer activity of MIL-100@Apa@MPN in a tumor-bearing mouse model. As shown in Figure 5A, the mice in the MIL-100@Apa@MPN group exhibited remarkable suppression of tumor proliferation, with

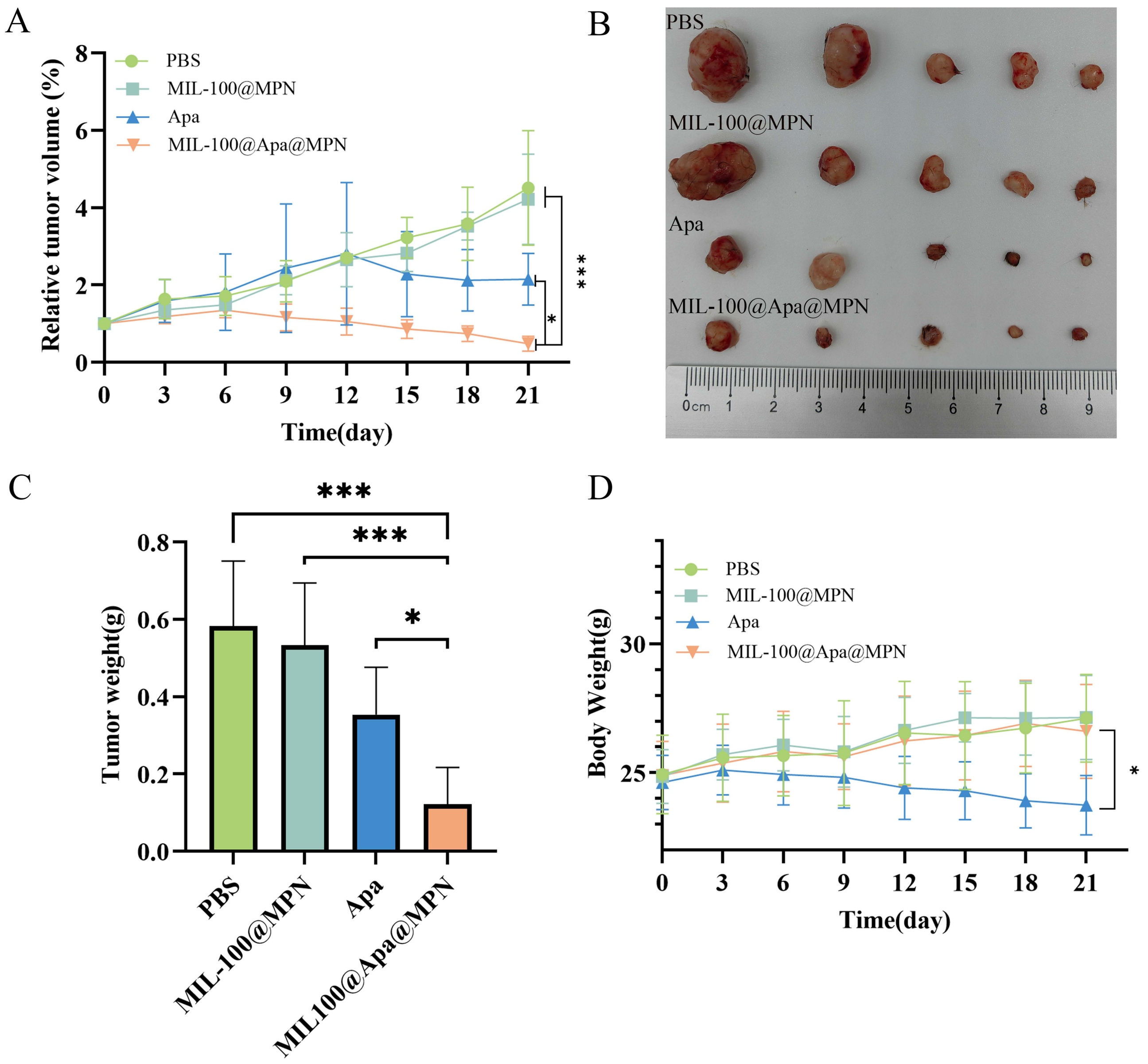

Figure 5 In vivo anti-tumor efficacy of the MIL-100@Apa@MPN in H22 tumor-bearing mice.

Notes: (**A**) Relative tumor volume curves in each group (n = 5). (**B**) Photographs of excised tumors in each group. (**C**) Tumor weight of the different groups (n = 5). (**D**) Body weight of mice in each group (n = 5). Data are presented as mean ± standard deviation (* $P < 0.05$, ** $P < 0.01$, *** $P < 0.001$).

Abbreviations: Apa, Apatinib; MPN, metal polyphenol network.

minimal augment in tumor volume observed over the experimental timeframe. Rapid tumor progression was detected in the PBS group, whereas MIL-100@MPN monotherapy inhibited tumor growth. Figure 5B depicts gross images of the excised tumors, further supporting the efficacy of MIL-100@Apa@MPN in inhibiting tumor growth. As shown in Figure 5C, tumor weights in the MIL-100@Apa@MPN group were significantly reduction ($P < 0.05$), providing further evidence of the favorable antitumor efficacy of the MIL-100@Apa@MPN.

Toxicology Investigation

The systemic adverse effects of the treatments was assessed by monitoring changes in body weight and conducting H&E staining on tissue sections of the organs. The mice administered with free Apa demonstrated the minimal extent of body weight augmentation ($P < 0.05$), whereas the weight trajectories of the MIL-100a@MPN group and MIL-100@Apa@MPN group closely resembled those of the PBS-treated mice (Figure 5D). In the MIL-100@Apa@MPN group, H&E of the vital organs exhibited no apparent indications of observation of hemorrhage, tissue edema (Figure 6A). Conversely, the Apa group exhibited notable organ toxicity, including liver necrosis, lung congestion and hemorrhage, and kidney edema (Figure 6A).

Histological and Immunohistochemical Analysis

H&E staining of tumor tissue samples obtained from various treatment groups showed the most pronounced level of damage to the cancer cells in the MIL-100@Apa@MPN administration group (Figure 6B). Ki-67 and CD31 immunohistochemical staining was conducted to evaluate tumor cell proliferation and tumor angiogenesis, respectively (Figure 7A). Furthermore, GPX4 and Caspase-3 immunostaining was conducted to assess ferroptosis and tumor cell apoptosis, respectively (Figure 7A). Compared with the control, the proportion of Ki-67 positive cells was significantly

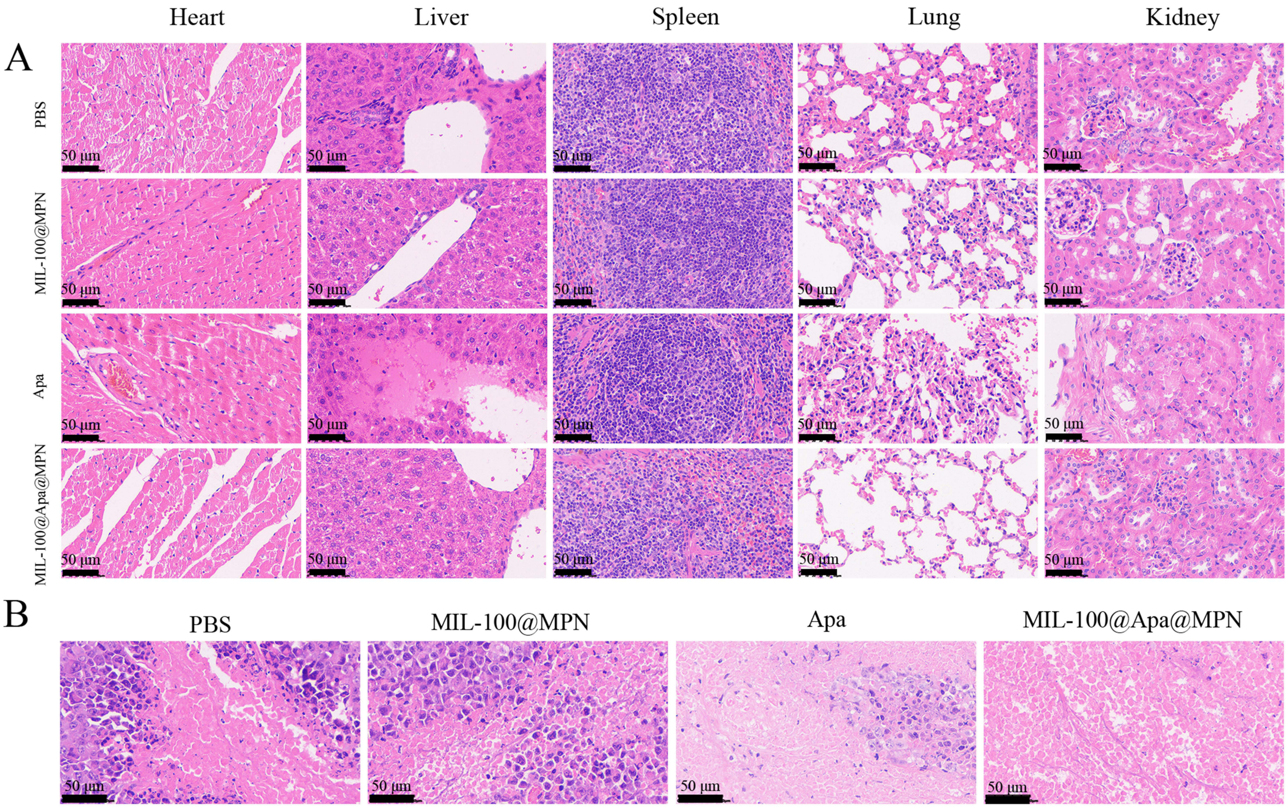

Figure 6 Representative images of H&E staining.

Notes: (**A**) Representative images of H&E staining of heart, liver, spleen, lung, and kidney sections in the different group. (**B**) H&E-stained histological sections of tumors of the different groups. Scale bar, 50 μm.

Abbreviations: Apa, Apatinib; MPN, metal polyphenol network.

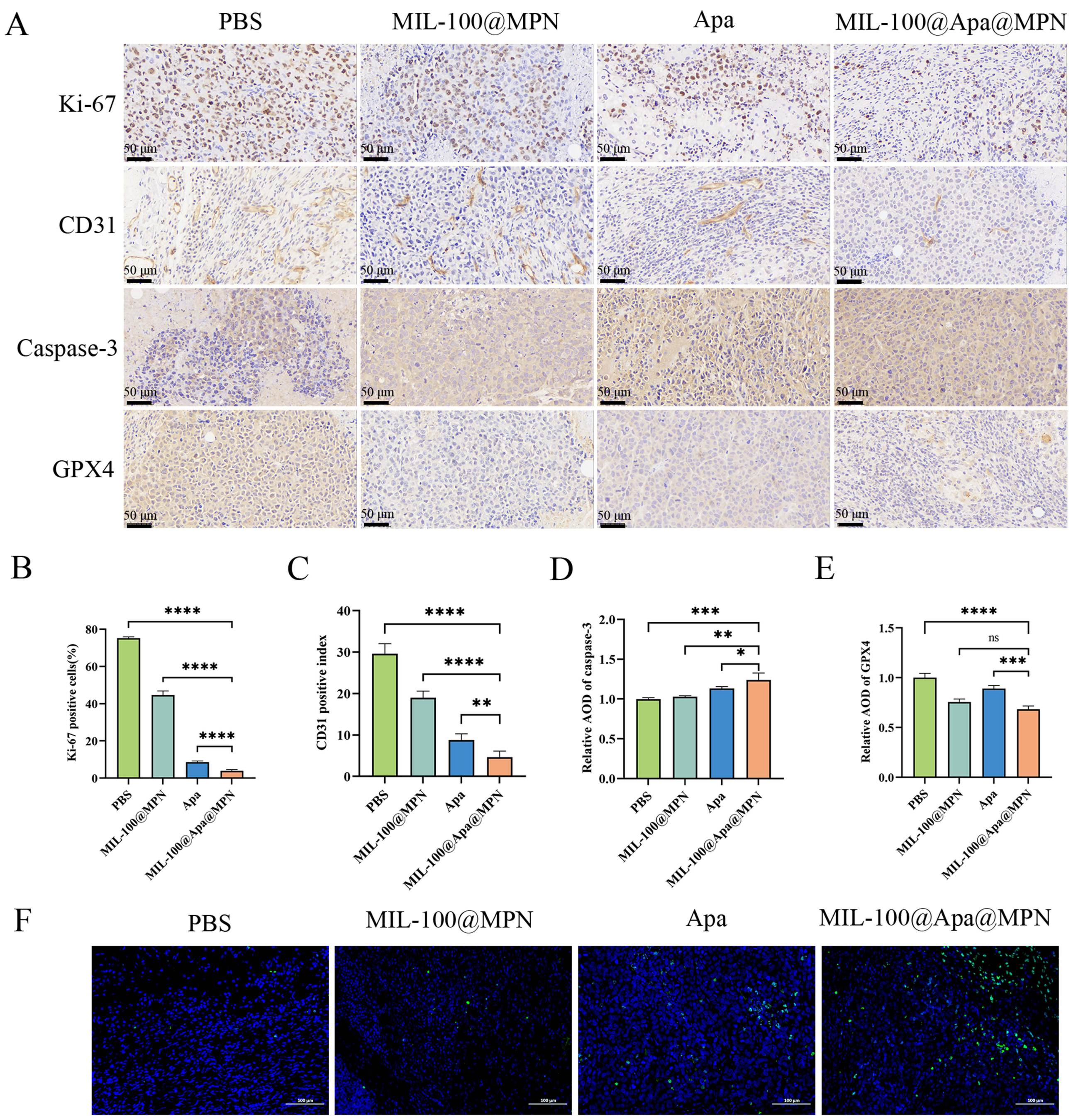

Figure 7 Representative images of immunohistochemical analysis of each group.

Notes: (**A**) Immunohistochemical analysis of tumor slices collected from tumor-bearing mice after different treatments. (**B**) The quantitative analysis of Ki-67 expression in each group. (**C**) The quantitative analysis of vascularization in each group. (**D**) The quantitative analysis of Caspase-3 expression in each group. (**E**) The quantitative analysis of GPX4 expression in each group. (**F**) TUNEL analysis of tumor slices collected from tumor-bearing mice after different treatments. Scale bar, 50 μm and 100μm (*$P < 0.05$, **$P < 0.01$, ***$P < 0.001$, **** $P < 0.0001$).

Abbreviations: Apa, Apatinib; MPN, metal polyphenol network; GPX4, glutathione peroxidase 4; Caspase-3, cysteinyl aspartate specific proteinase 3; TUNEL, TdT-mediated dUTP nick-end labeling.

reduced in the MIL-100@Apa@MPN group, suggesting that MIL-100@Apa@MPN effectively inhibited tumor proliferation (Figure 7B). In addition, the microvessel density (MVD) positive for CD31 in group MIL-100@Apa@MPN was markedly reduced (Figure 7C), indicating that group MIL-100@Apa@MPN effectively suppressed angiogenesis. The average optical density (AOD) of caspase-3 staining in the MIL-100@Apa@MPN and free Apa groups was significantly elevated ($P < 0.05$) (Figure 7D). Furthermore, the AOD in the MIL-100@Apa@MPN group was the highest. These findings indicate that MIL-100@Apa@MPN promotes apoptosis. In addition, the AOD of GPX4 staining in the MIL-100@Apa@MPN and MIL-100@MPN groups was significantly reduced (Figure 7E). These results suggested that MIL-100@Apa@MPN effectively promotes cellular ferroptosis. TUNEL assays also showed the most pronounced level of apoptosis in the MIL-100@Apa@MPN group (Figure 7F).

Discussion

HCC, characterized by high morbidity and mortality rates, poses a significant global health threat.[25] Targeted therapy is one of the principal strategies for the treatment of cancer. However, traditional targeted therapy often faces challenges associated with non-specific distribution and uncontrolled drug release, resulting in substantial systemic toxicity.[26] Approaches to the development of more advanced targeted drug delivery systems have been gaining increasing attention. These systems are designed to deliver drugs directly to the target site, thereby improving specificity and therapeutic efficacy while at the same time reducing systemic toxicity and side-effects and enhanced specificity compared to systemic drug-delivery. Nanoparticle-based targeted drug delivery systems have gained recognition as an effective approach that mitigates the high degree of systemic toxicity associated with chemotherapeutic agents. Furthermore, investigations into the multifunctional NPs as drug-delivery platforms is expanding, introducing a novel approach to tumor treatment. Multiple studies have provided increasing evidence that MOFs, known for their controlled and sustained drug-release capabilities and reduced toxicity, hold promise for tumor therapy.[27–33]

Nonetheless, numerous hydrophobic antitumor agents, like Apa, exhibit poor water solubility and limited dispersibility in aqueous environments. Consequently, our study involved the encapsulation of Apa within MOFs to enhance its bioavailability and mitigate systemic toxicity. In this context, given the biologically non-toxic nature of MPN, we firstly employed MPN-coated iron-based MOFs as a drug-delivery platform aimed at cancer targeting in the treatment of HCC.

The PXRD pattern was highly consistent with the simulated patterns derived from the single-crystal data of MIL-100, confirming the adoption of the MIL-100 structure by the nanoparticle and the high purity of the prepared sample. The substantial loading capacity of Apa can be attributed to the electrostatic interaction between Apa and MIL-100, along with the mesoporous structure of MIL-100. The successful synthesis of MIL-100@Apa@MPN was verified through TEM images, HRTEM images, DLS size measurements, and zeta potential values. The FT-IR spectroscopy analysis showed that some of the carboxylic groups that were initially bound to Fe^{3+} were exposed as a result of the coordination bond formed between the polyphenol groups of TA and Fe^{3+} of MIL-100, leading to the emergence of a carboxylic stretching band at 1,710 cm^{-1}.[34] In the case of the MIL-100@MPN membrane, we observed a noticeable increase in peak intensity at 1,201 and 1,037 cm^{-1}, suggesting enhanced anchoring of TA molecules on the surface of the MIL-100 membrane via TA-Fe coordination cross-linking.[35] The emergence of new absorption bands at approximately 621 cm^{-1} were attributed to Fe-O lattice vibrations, further validating the interaction between TA and Fe^{3+}.[36,37] XPS characterizations showing that the characteristic peaks of Fe^{3+} species at 716.6 and 729.6 eV further confirmed Fe^{3+} as the predominant form of Fe in MIL-100 and MIL-100@MPN. The additional peaks observed at 709.7 and 723.1 eV in MIL-100@MPN representative the presence of Fe^{2+} species indicated that ferrous Fe^{2+} was generated as a result of the coordination reaction between gallate in TA and ferric Fe^{3+}.[38–40] The presence of Fe^{2+} in the MPN structure imparts the NPs with reductive properties, which are advantageous for the peroxidase-like activity of the NPs. This characteristic enhances the ability of the NPs to catalyze the Fenton reaction, which is widely acknowledged as a mechanism that converts intracellular H_2O_2 into hydroxyl radicals (·OH) and ROS.[41–43] These substances exert cytotoxic effects on tumor cells.

The outcomes of the in vitro release study demonstrated the release of Apa was from MIL-100@MPN, with a controlled release profile. At pH 7.4, the rate of Apa release was gradual, with 42.31% accumulated over 72 h. At pH 5.0, the release of Apa was comparatively rapid, with an accumulated release of 73.72% in 72 h. This phenomenon can be ascribed to the pH-responsive mechanism of the drug-delivery system. In an acidic milieu, decomposition of the MPN shell facilitates the discharge of MIL-100@Apa and liberation of the drug-loaded MOF. Such pH-responsive behavior and gradual liberation of Apa from MIL-100, coupled with the Fenton reaction of Fe^{2+} generated through catabolism, culminates in drug accumulation within the tumor microenvironment. This protracted presence contributes to sustained tumor growth suppression, synergizing with ferroptosis to enhance therapeutic outcomes. The in vitro cytotoxicity evaluation revealed that MIL-100@MPN exhibited inherent antitumor properties, potentially associated with the induction of ferroptosis subsequent to the degradation of MPN and MIL-100. This inference was corroborated by the enhanced cellular proliferation in the presence of ferroptosis inhibitors such as Vit-E, and Fer-1. At the same time, we also detected the GSH and H_2O_2 concentration of the MIL-100@MPN and MIL-100@Apa@MPN groups, confirming the occurrence of the Fenton reaction. The MIL-100@Apa@MPN exhibited superior antitumor efficacy compared to the free drug, which can potentially be ascribed to the enhanced cellular uptake efficiency of the encapsulated drug by HepG2 cells and synergistic effect of ferroptosis. Moreover, in vivo investigations substantiated the potent therapeutic efficacy of MIL-100@Apa@MPN, highlighting its ability to impede tumor progression and extend the survival of mice. These findings could potentially related to the high drug-loading capacity of MIL-100@MPN and the synergistic effect on the targeted drug release drug combined with ferroptosis. Interestingly, the MIL-100@MPN group demonstrates substantial cytotoxicity within 24 hours. This observation may be attributed to the ferroptosis in the MIL-100@MPN group, which inhibited tumor growth, demonstrating significant early-stage inhibition but no significant late-stage tumor suppression.[44] In addition, IHC analysis of tumor tissues dealt with MIL-100@Apa@MPN showed lower numbers of both Ki-67 and CD31-positive MVDs, indicating significant inhibition of tumor proliferation and angiogenesis. The underlying anticancer mechanism was revealed by GPX4, caspase-3 and TUNEL staining of dissected tumor tissues. Tissues from mice treated with MIL-100@Apa@MPN showed higher caspase-3 expression, suggesting significant induction of apoptosis, as compared to the other three groups. Since ferroptosis can suppress the phospholipid peroxidase GPX4, leading to a fatal buildup of lipid peroxides, GPX4 was employed as a marker of this process.[45] The MIL-100@Apa@MPN group exhibited reduced GPX4 expression, signifying the occurrence of ferroptosis. Furthermore, the TUNEL assay provided further evidence that MIL-100@Apa@MPN significantly enhances apoptosis.

The biocompatibility and non-toxic nature of drug-loaded delivery systems are crucial considerations for their clinical utility. Compared to the Apa group, the important organs H&E staining of MIL-100@Apa@MPN show significant low toxicity. Yu et al synthesized a comparable MPN-coated substance comprising a blend of MPN and the metal-organic nanostructure for the treatment of gastric cancer.[37] Comprehensive in vivo investigations have illustrated that this drug-delivery system exhibits favorable biocompatibility and minimal toxicity toward vital organs. In accordance with these findings, our research revealed that MIL-100@Apa@MPN mitigated the adverse effects of Apa without inducing substantial systemic toxicity, thereby positioning it as a hopeful localized therapy delivery system.

Analogous investigations on MOFs as drug-delivery platforms have been undertaken previously. Huang et al developed a MOF-based drug-delivery system capable of effectively transporting chemotherapeutic agents to tumors. Their results indicated that the MOF-based drug-delivery system initiated a Fenton reaction within the tumor micro-environment, with effective tumor suppression and minimal side-effects.[46] In a separate investigation, Wang et al synthesized NPs comprising MIL-100 as the shell and carbon-coated iron oxide as the core to create a theranostic platform for dual-modal imaging-guided cancer chemotherapy using the low-toxicity Chinese medicine DHA.[47] Similarly, a different study demonstrated a more conventional method for established a multifunctional synergistic MOF-based therapeutic medical nanoplatform by employing PVP-modified PPy as a nucleation site within MIL-100.[48] The drug-delivery system based on Apa-loaded metal-organic framework established in this study is pH-responsive and can be degraded in the acidic tumor microenvironment, which facilitates the slow release of the drug at this site. Furthermore, the drug-delivery system is not only easy to employ, but also simple to produce and amenable to large-scale production, thereby holding significant promise for clinical deployment. In addition, the MPN coating has the advantages of good biodegradability, convenient encapsulation, and few side-effects, transforming it into a secure and efficient drug delivery system. In addition, this drug-delivery system facilitates the release of Fe^{2+} to induce ferroptosis and synergize with chemotherapy, thereby enhancing the therapeutic effect on tumors. However, further studies are needed to examine the intricate mechanisms in depth and to optimize the MOF preparation and nanoparticle DL.

Conclusion

In summary, the MIL-100@Apa@MPN drug-delivery system was developed to induce ferroptosis that acts synergistically with targeted therapy for the treatment of HCC. We prepared MIL-100 and conjugated it with Apa and combined it with TA to generate MPN, constructing a metal-organic framework drug-delivery system with good safety, slow-release properties, pH-responsivity, and enhanced therapeutic effects. Apa has the ability to bind specifically to VEGFR2. The high concentration of GSH within the tumor tissue facilitates the conversion of Fe^{3+} present in MIL-100 to Fe^{2+}. This reduction process leads to the generation of highly cytotoxic hydroxyl ·OH through the Fenton reaction, which can be utilized for effective ferroptosis therapy. Consequently, the attainment of synergistic cancer therapy, predominantly encompassing targeted therapy and ferroptosis therapy, may be realized. Therefore, MIL-100@Apa@MPN is a promising drug-delivery system with heightened level of biological safety and enhanced therapeutic effects. We posit that this investigation holds the potential to lay the groundwork for the development of innovative nanoplatforms capable of responding to pH. Such advancements are expected to yield improved therapeutic outcomes for HCC in forthcoming times.

Acknowledgments

All authors made a significant contribution to the work reported, whether that is in the conception, study design, execution, acquisition of data, analysis and interpretation, or in all these areas; took part in drafting, revising or critically reviewing the article; gave final approval of the version to be published; have agreed on the journal to which the article has been submitted; and agree to be accountable for all aspects of the work.

Funding

This work was supported by the Key Research and Development Project of the Science & Technology Department of Sichuan Province (Nos.2023YFQ0101), Sichuan Science and Technology Program (Nos.2022YFS0625) and Luzhou Science and Technology and Talent Work Bureau (Nos.2022-SYF-55).

Disclosure

The authors have no relevant financial or non-financial interests to disclose.

References

1. Sung H, Ferlay J, Siegel RL, et al. Global cancer statistics 2020: GLOBOCAN estimates of incidence and mortality worldwide for 36 cancers in 185 countries. *CA Cancer J Clin*. 2021;71(3):209–249. doi:10.3322/caac.21660
2. Forner A, Reig M, Bruix J. Hepatocellular carcinoma. *Lancet*. 2018;391(10127):1301–1314. doi:10.1016/s0140-6736(18)30010-2
3. Hicklin DJ, Ellis LM. Role of the vascular endothelial growth factor pathway in tumor growth and angiogenesis. *J Clin Oncol*. 2005;23(5):1011–1027. doi:10.1200/jco.2005.06.081
4. Lee JE, Kim KL, Kim D, et al. Apatinib-loaded nanoparticles suppress vascular endothelial growth factor-induced angiogenesis and experimental corneal neovascularization. *Int J Nanomed*. 2017;12:4813–4822. doi:10.2147/ijn.S135133
5. Roskoski Jr R. Small molecule protein kinase inhibitors approved by regulatory agencies outside of the United States. *Pharmacol Res*. 2023;194:106847. doi:10.1016/j.phrs.2023.106847
6. Qin S, Li Q, Gu S, et al. Apatinib as second-line or later therapy in patients with advanced hepatocellular carcinoma (AHELP): A multicentre, double-blind, randomised, placebo-controlled, Phase 3 trial. *Lancet Gastroenterol Hepatol*. 2021;6(7):559–568. doi:10.1016/s2468-1253(21)00109-6
7. Zheng Z, Liu Z, Zhang H, et al. Efficacy and safety of apatinib in advanced hepatocellular carcinoma: A multicenter real world retrospective study. *Front Pharmacol*. 2022;13:894016. doi:10.3389/fphar.2022.894016
8. Zhang L, Zhang K, Wang C, et al. Advances and prospects in metal-organic frameworks as key nexus for chemocatalytic hydrogen production. *Small*. 2021;17(52):e2102201. doi:10.1002/smll.202102201
9. Wu MX, Yang YW. Metal-organic framework (mof)-based drug/cargo delivery and cancer therapy. *Adv Mater*. 2017;29(23). doi:10.1002/adma.201606134
10. Shen Y, Pan T, Wang L, Ren Z, Zhang W, Huo F. Programmable logic in metal-organic frameworks for catalysis. *Adv Mater*. 2021;33(46):e2007442. doi:10.1002/adma.202007442
11. Zheng Q, Liu X, Zheng Y, et al. The recent progress on metal-organic frameworks for phototherapy. *Chem Soc Rev*. 2021;50(8):5086–5125. doi:10.1039/d1cs00056j
12. Horcajada P, Chalati T, Serre C, et al. Porous metal-organic-framework nanoscale carriers as a potential platform for drug delivery and imaging. *Nat Mater*. 2010;9(2):172–178. doi:10.1038/nmat2608
13. Deng K, Hou Z, Li X, et al. Aptamer-mediated up-conversion core/MOF shell nanocomposites for targeted drug delivery and cell imaging. *Sci Rep*. 2015;5:7851. doi:10.1038/srep07851
14. Qin W, Silvestre ME, Li Y, Franzreb M. High performance liquid chromatography of substituted aromatics with the metal-organic framework MIL-100(Fe): Mechanism analysis and model-based prediction. *J Chromatogr A*. 2016;1432:84–91. doi:10.1016/j.chroma.2016.01.006
15. Zheng DW, Lei Q, Zhu JY, et al. Switching apoptosis to ferroptosis: Metal-organic network for high-efficiency anticancer therapy. *Nano Lett*. 2017;17(1):284–291. doi:10.1021/acs.nanolett.6b04060
16. Bao W, Liu X, Lv Y, et al. Nanolongan with multiple on-demand conversions for ferroptosis-apoptosis combined anticancer therapy. *ACS Nano*. 2019;13(1):260–273. doi:10.1021/acsnano.8b05602

17. Shen Z, Song J, Yung BC, Zhou Z, Wu A, Chen X. Emerging strategies of cancer therapy based on ferroptosis. *Adv Mater*. 2018;30(12):e1704007. doi:10.1002/adma.201704007
18. Zhang C, Liu X, Jin S, Chen Y, Guo R. Ferroptosis in cancer therapy: A novel approach to reversing drug resistance. *Mol Cancer*. 2019;21(1):47. doi:10.1186/s12943-022-01530-y
19. Xia L, Gong M, Zou Y, et al. Apatinib induces ferroptosis of glioma cells through modulation of the VEGFR2/Nrf2 pathway. *Oxid Med Cell Longev*. 2022;2022:9925919. doi:10.1155/2022/9925919
20. Zhang L, Wan SS, Li CX, Xu L, Cheng H, Zhang XZ. An adenosine triphosphate-responsive autocatalytic Fenton nanoparticle for tumor ablation with self-supplied h(2)o(2) and acceleration of Fe(III)/Fe(II) conversion. *Nano Lett*. 2018;18(12):7609–7618. doi:10.1021/acs.nanolett.8b03178
21. Fang Y, Yang Z, Li H, Liu X. MIL-100(Fe) and its derivatives: From synthesis to application for wastewater decontamination. *Environ Sci Pollut Res Int*. 2020;27(5):4703–4724. doi:10.1007/s11356-019-07318-w
22. Zhang F, Jin Y, Shi J, Zhong Y, Zhu W, El-Shall MS. Polyoxometalates confined in the mesoporous cages of metal–organic framework MIL-100 (Fe): Efficient heterogeneous catalysts for esterification and acetalization reactions. *Chem Eng J*. 2015;269:236–244. doi:10.1016/j.cej.2015.01.092
23. Li X, Guo W, Liu Z, Wang R, Liu H. Fe-based MOFs for efficient adsorption and degradation of acid Orange 7 in aqueous solution via persulfate activation. *Appl Surf Sci*. 2016;369:130–136. doi:10.1016/j.apsusc.2016.02.037
24. Fang R, Luque R, Li Y. Efficient one-pot fructose to DFF conversion using sulfonated magnetically separable MOF-derived Fe 3 O 4 (111) catalysts. *Green Chem*. 2017;19(3):647–655. doi:10.1039/C6GC02018F
25. Shah PA, Patil R, Harrison SA. NAFLD-related hepatocellular carcinoma: The growing challenge. *Hepatology*. 2023;77(1):323–338. doi:10.1002/hep.32542
26. Aggarwal D, Yang J, Salam MA, et al. Antibody-drug conjugates: The paradigm shifts in the targeted cancer therapy. *Front Immunol*. 2023;14:1203073. doi:10.3389/fimmu.2023.1203073
27. Zhao D, Timmons DJ, Yuan D, Zhou HC. Tuning the topology and functionality of metal-organic frameworks by ligand design. *Acc Chem Res*. 2011;44(2):123–133. doi:10.1021/ar100112y
28. Corma A, García H, Llabrés I Xamena FX. Engineering metal organic frameworks for heterogeneous catalysis. *Chem Rev*. 2010;110(8):4606–4655. doi:10.1021/cr9003924
29. Keskin S, Kızılel S. Biomedical applications of metal organic frameworks. *Ind Eng Chem Res*. 2011;50(4):1799–1812. doi:10.1021/ie101312k
30. Yang XL, Chen X, Hou GH, Guan RF, Shao R, Xie MH. A multiresponsive metal–organic framework: Direct chemiluminescence, photoluminescence, and dual tunable sensing applications. *Adv Funct Mater*. 2016;26(3):393–398. doi:10.1002/adfm.201503935
31. Kaur R, Kim K-H, Paul A, Deep A. Recent advances in the photovoltaic applications of coordination polymers and metal organic frameworks. *J Mater Chem A*. 2016;4(11):3991–4002. doi:10.1039/C5TA09668E
32. Li H, Guo K, Wu C, et al. Controlled and targeted drug delivery by a UV-responsive liposome for overcoming chemo-resistance in non-Hodgkin lymphoma. *Chem Biol Drug Des*. 2015;86(4):783–794. doi:10.1111/cbdd.12551
33. He Q, Gao Y, Zhang L, et al. A pH-responsive mesoporous silica nanoparticles-based multi-drug delivery system for overcoming multi-drug resistance. *Biomaterials*. 2011;32(30):7711–7720. doi:10.1016/j.biomaterials.2011.06.066
34. Aromal SA, Philip D. Facile one-pot synthesis of gold nanoparticles using tannic acid and its application in catalysis. *Physica E Low Dimens Syst Nanostruct*. 2012;44(7–8):1692–1696. doi:10.1016/j.physe.2012.04.022
35. Wang R, Zhao X, Lan Y, Liu L, Gao C. In situ metal-polyphenol interfacial assembly tailored superwetting PES/SPES/MPN membranes for oil-in-water emulsion separation. *J Membr Sci*. 2020;615:118566. doi:10.1016/j.memsci.2020.118566
36. Xiao L, Li J, Brougham DF, et al. Water-soluble superparamagnetic magnetite nanoparticles with biocompatible coating for enhanced magnetic resonance imaging. *ACS Nano*. 2011;5(8):6315–6324. doi:10.1021/nn201348s
37. Yu J, Guo Z, Yan J, et al. Gastric acid-responsive ros nanogenerators for effective treatment of helicobacter pylori infection without disrupting homeostasis of intestinal flora. *Adv Sci*. 2023;10(20):e2206957. doi:10.1002/advs.202206957
38. Zhao H, Wang Y, Wang Y, Cao T, Zhao G. Electro-Fenton oxidation of pesticides with a novel Fe3O4@ Fe2O3/activated carbon aerogel cathode: High activity, wide pH range and catalytic mechanism. *Appl Catal B*. 2012;125:120–127. doi:10.1016/j.apcatb.2012.05.044
39. Grosvenor A, Kobe B, Biesinger MC, McIntyre N. Investigation of multiplet splitting of Fe 2p XPS spectra and bonding in iron compounds. *Surf Interface Anal*. 2004;36(12):1564–1574. doi:10.1002/sia.1984
40. Lv H, Zhao H, Cao T, Qian L, Wang Y, Zhao G. Efficient degradation of high concentration azo-dye wastewater by heterogeneous Fenton process with iron-based metal-organic framework. *J Mol Catal a Chem*. 2015;400:81–89. doi:10.1016/j.molcata.2015.02.007
41. Fu LH, Qi C, Lin J, Huang P. Catalytic chemistry of glucose oxidase in cancer diagnosis and treatment. *Chem Soc Rev*. 2018;47(17):6454–6472. doi:10.1039/c7cs00891k
42. Liu F, Lin L, Zhang Y, et al. A tumor-microenvironment-activated nanozyme-mediated theranostic nanoreactor for imaging-guided combined tumor therapy. *Adv Mater*. 2019;31(40):e1902885. doi:10.1002/adma.201902885
43. Wang P, Shi Y, Zhang S, et al. Hydrogen peroxide responsive iron-based nanoplatform for multimodal imaging-guided cancer therapy. *Small*. 2019;15(4):e1803791. doi:10.1002/smll.201803791
44. Wan X, Song L, Pan W, et al. Tumor-targeted cascade nanoreactor based on metal-organic frameworks for synergistic ferroptosis-starvation anticancer therapy. *ACS Nano*. 2020;14(9):11017–11028. doi:10.1021/acsnano.9b07789
45. Liang D, Feng Y, Zandkarimi F, et al. Ferroptosis surveillance independent of GPX4 and differentially regulated by sex hormones. *Cell*. 2023;186(13):2748–2764.e22. doi:10.1016/j.cell.2023.05.003
46. Huang R, Liu W, Zhang Q, et al. Laser-induced combinatorial chemotherapeutic, chemodynamic, and photothermal therapy for hepatocellular carcinoma based on oxaliplatin-loaded metal-organic frameworks. *ACS Appl Mater Interfaces*. 2023;15(3):3781–3790. doi:10.1021/acsami.2c19305
47. Wang D, Zhou J, Chen R, et al. Magnetically guided delivery of DHA and Fe ions for enhanced cancer therapy based on pH-responsive degradation of DHA-loaded Fe3O4@C@MIL-100(Fe) nanoparticles. *Biomaterials*. 2016;107:88–101. doi:10.1016/j.biomaterials.2016.08.039
48. Zhu YD, Chen SP, Zhao H, et al. PPy@MIL-100 nanoparticles as a ph- and near-ir-irradiation-responsive drug carrier for simultaneous photothermal therapy and chemotherapy of cancer cells. *ACS Appl Mater Interfaces*. 2016;8(50):34209–34217. doi:10.1021/acsami.6b11378